Flow and mass transfer in liquid-fluidized spherical rings

J.J. Derksen

School of Engineering, University of Aberdeen, Aberdeen AB24 3UE, UK

jderksen@abdn.ac.uk

Submitted to ChERD – May 2026

Revision submitted June 2026

Accepted June 2026

Abstract

Spherical rings are spheres with a concentric cylindrical borehole. We assess such particles for their capacity of achieving liquid-solid mass transfer under dense, fluidized conditions with the mass transfer interface restricted to the inner cylindrical bore surface. For this we perform three-dimensional particle resolved flow simulations in fully periodic domains using the lattice-Boltzmann method, including immersed boundaries for achieving no-slip at solid surfaces. The solids packing fractions are in the range 0.49 to 0.58; the ratios of sphere over bore diameter are between 0.42 and 0.61; the Archimedes number of the spherical ring particles has been varied from $2.8 \cdot 10^3$ to $1.1 \cdot 10^4$. Average Sherwood numbers as well as volumetric mass transfer coefficients have been estimated based on the (resolved) flow inside the cylindrical bore of each particle and make use of solutions to the Graetz problem. It is shown to what extent fluidization instabilities and particle orientation relative to the direction of gravity influence bore throughflow and consequently mass transfer.

Keywords

Spherical ring; liquid-solid fluidization; particle-resolved simulation; mass transfer.

1. INTRODUCTION

Compared to gas fluidization, liquid fluidization is a relatively minor area in (chemical) engineering research. This is most likely due to the much wider application and the often much larger scales of operation of gas fluidization making it economically much more relevant and more challenging from perspectives such as scale-up, process control and optimization [Kunii and Levenspiel, 1993]. However, there also are numerous and wide-ranging applications of liquid fluidized systems with examples covering freeze crystallization processes [Pronk et al., 2006], wastewater treatment [Seepma et al., 2025], bioreactors [Koerich and Machado da Rosa, 2021], battery electrodes for fast charging [Adelusi et al., 2020], and mineral processing [Syed et al., 2018]. In many of these applications, achieving high levels of (reactive) mass transfer between solid and liquid is a primary objective. In catalytic reactors, the solids carry catalyst at their surface and/or in their pores, thereby by enabling heterogeneous reactions with the reagents supplied – and product removed – through the liquid phase [Froment et al., 2011].

The research we present in the current paper is inspired by catalytic particles interacting with a continuous liquid phase. The perceived fragility of the catalytic material means that we want to explore the use of spherical ring-shaped particles (see Figure 1 for an impression) with the catalytic material only applied to the inner cylindrical surface so that collisions between particles will not damage and/or wear off the catalytic coating. Attrition due to particle-particle collisions in fluidization is a main source of catalyst degradation in – among more – fluid catalytic processes [Bartholomew 2001]. The issue we want to address here is how to estimate mass transfer rates at the inner surfaces of a fluidized collection of spherical rings and how these rates depend on geometrical and operating conditions such as solids volume fractions, liquid and solids properties, and fluidization velocities. We realize that key answers to such questions will primarily need to be established by careful experimentation. In this paper, however, we focus on numerical modeling. This we do to try and identify rate limiting steps in mass transfer and how they depend on process parameters. We believe that detailed modeling of the systems at hand will support our understanding and subsequently be beneficial for design of experiment and for process design.

The physics of gas and liquid fluidization share many concepts, very prominent ones being the momentum exchange between the fluid (gas or liquid) and solids phases as well as the momentum exchange between solids (particle-particle collisions; granular stresses). They largely determine the stability and mode of operation and thereby the performance of the fluidized bed [Sundaresan, 2003]. Timescales related to these momentum exchange mechanisms in fluidization differ between different types of systems and depend – among more – on the properties of the fluid(s) involved. A distinctive difference between liquid and gas is their density which – depending on circumstances such as pressure and temperature – is two to three orders of magnitude larger for liquids than for gases. This translates into liquid fluidized particles having much smaller Stokes numbers than gas fluidized particles which in turn means that liquid fluidized particle configurations adapt faster to varying flow conditions. This has profound consequences for e.g. hydrodynamic interaction forces [Wen and Yu, 1966; Van der Hoef et al., 2005; Rubinstein et al., 2016]. Where in gas fluidization drag force correlations based on simulations of flow through fixed random assemblies of particles (as e.g. in [Van der Hoef et al., 2006]) are appropriate, this might less be so for liquid fluidization, as demonstrated in [Rubinstein et al., 2016]. In addition, the relative importance in liquids of other hydrodynamic forces such as added mass and lift as compared to drag is expected to be larger than in gases [Clift et al.,1978].

The fact that we are dealing with non-spherical particles, where the flow inside the cylindrical bores needs to be resolved, plus the fact that we expect that drag-only hydrodynamic forces are not sufficient to capture the fluidization dynamics, makes us choose, in the first instance, for particle-resolved simulations. Given that these are computationally expensive on a per-particle basis (they need computational grids finer by at least one order of magnitude compared to particle sizes – therefore $O\left(10^3 - 10^4\right)$ grid nodes per particle) the flow systems that can be studied are small in terms of numbers of particles and thus in physical space. By employing periodic boundary conditions, the simulations are representative of much larger systems, albeit away from walls and/or local internal structures.

The aims of this paper are (1) to establish a methodology for simulating liquid-fluidized systems of spherical-ring-shaped particles at high spatial and temporal resolution, (2) to characterize their flow dynamics, and (3) to relate that to the mass transfer potential of the cylindrical bore surfaces. The (design) variables considered are the solids packing fraction, the bore diameter relative to the sphere diameter, and the fluidization velocity (through variations of the Archimedes number). This paper builds upon a previous paper [Derksen, 2023] on liquid fluidization of solid and hollow cylindrical particles. In that paper, as well as in the current one, wave instabilities develop in the fluidized beds. One of the more specific objectives is to investigate the effect of those instabilities on mass transfer rates.

2. FLOW SYSTEM

The flow domain is a fully periodic rectangular cuboid (with a Cartesian x, y, z coordinate system) of size $nx \times ny \times nz$. It contains rigid solid particles with density ρ_p and Newtonian liquid with density $\rho < \rho_p$ and kinematic viscosity ν. The particles are spherical rings (see Figures 1 and 2) with diameter d and bore diameter d_i. The height h (as defined in Figure 2) of the inner cylindrical surface is $h = \sqrt{d^2 - d_i^2}$; the particle volume is $V_p = \frac{\pi}{6}\left(d^2 - d_i^2\right)^{1.5} = \frac{\pi}{6}h^3$; the moment of inertia matrix is

$$\mathbf{I} = \rho_p V_p \begin{bmatrix} d^2/4 - 3h^2/20 & 0 & 0 \\ 0 & d^2/8 - h^2/40 & 0 \\ 0 & 0 & d^2/8 - h^2/40 \end{bmatrix}$$

in a Cartesian coordinate system (x_1, x_2, x_3) attached to the spherical ring with the first (x_1) coordinate along the centerline of the bore. With n identical particles the overall solids volume fraction is defined as $\langle \phi \rangle = nV_p / (nx \cdot ny \cdot nz)$. We introduce a second overall volume fraction that we term packing fraction $\langle \phi_{pck} \rangle = n\left(V_p + \frac{\pi}{4}hd_i^2\right) / (nx \cdot ny \cdot nz)$, i.e. we include the bore volume in this fraction so that it is recognized that this inner cylindrical volume ($\frac{\pi}{4}hd_i^2$) is too narrow to lodge any other particle. Note that $\langle \phi_{pck} \rangle$ does not include the spherical cap volumes (each equal to $\frac{1}{3}\pi c^2\left(\frac{3}{2}d - c\right)$ with c defined in Figure 2).

Gravity points in the negative z direction. The domain sizes are $nx = ny = 12d$ and $nz = 24d$. Given the full periodicity of the flow system, we explicitly need to maintain an overall force balance. For the *z*-direction, the net gravity (downward) force on the solids needs to be compensated for by an upward body force (i.e. a pressure gradient) on the fluid $\mathbf{f} = (\rho_m - \rho) g \mathbf{e}_z$ [Derksen and Sundaresan, 2007] with $\rho_m = \rho_p \langle \phi \rangle + \rho(1 - \langle \phi \rangle)$ the mixture density, g gravitational acceleration, and $\mathbf{e}_z$ the unit vector in *z*-direction. An Archimedes number is defined as $\mathrm{Ar} = (\gamma - 1) g V_p / \nu^2$ with $\gamma = \rho_p / \rho$. The values for the Archimedes number are derived from a system with particle a diameter of about $d \approx 1$ mm, bore diameter of $d_i \approx 0.5$ mm, liquid viscosity of $\nu \approx 1.4 \cdot 10^{-6}$ m^2/s, density ratio $\gamma \approx 4$ and $g = 9.8$ m/s^2; then $\mathrm{Ar} \approx 5 \cdot 10^3$.

Parameters have been varied such that we cover the following ranges/values: Ar from $2.82 \cdot 10^3$ to $1.13 \cdot 10^4$; three packing fractions $\langle \phi_{pck} \rangle = 0.494$, 0.537 and 0.583. The number of particles in a simulation ranged from $n \approx 3300$ to 4100. We study three different spherical ring type particles that have volume over solid sphere volume $V_p / \left(\frac{\pi}{6} d^3 \right)$ of 0.75, 0.67 and 0.50 respectively (these have diameter ratios $d_i / d = 0.418$, 0.487 and 0.608 respectively). We compare these particles so that they have the same Archimedes number $\mathrm{Ar} = (\gamma - 1) g V_p / \nu^2$, i.e. if we reduce $V_p / \left(\frac{\pi}{6} d^3 \right)$ by making a wider bore, we increase their density and thus γ accordingly.

3. SIMULATION SETUP

The current paper builds upon earlier work when it comes to the numerical methods used as well as their applications. Previous work on settling and fluidization of hollow particles dealt with hollow cylinders rather than spheres [Derksen, 2013].

A lattice-Boltzmann (LB) [Succi, 2001] flow solver has been used. It represents the flow field (in terms of velocity and pressure) on a three-dimensional, uniform, cubic grid with spacing Δ and evolves the flow with a time step Δt. The specific LB scheme we use was introduced by Somers and Eggels [Somers, 1993; Eggels and Somers, 1995]. In the context of LB simulations, we have developed over the years (starting with [Derksen and Van den Akker, 1999]) an immersed boundary (IB) method to apply no-slip boundary conditions at solid surfaces that are not necessarily aligned with the grid and move relative to the grid. With this IB method we impose no-slip at the spherical ring surfaces. Since the IB method is based on forcing the fluid to adapt its velocity to that of the solid surfaces, it directly provides a hydrodynamic force distribution over the surface of each particle. Integrating this distribution for each particle allows one to calculate the hydrodynamic force and torque acting on each particle. These forces and torques are included in the equations of linear and rotational motion that we solve for every particle. This achieves a tight coupling between fluid and solids dynamics: the fluid flow moves the particles, and the particles' location and velocity provide boundary conditions for the fluid flow.

At a more detailed level, a few procedures and assumptions are worth highlighting, with further details to be found in earlier papers that we refer to for each of these procedures.

The IB method uses closely spaced marker points (spacing $\approx 0.7\Delta$) on the solid surfaces. At these points we apply forces to the fluid so that its local velocity matches the solid surface local velocity [Derksen and Van den Akker,1999; Ten Cate et al., 2002]. Solid surface marker points are also used for detecting close-range interactions between particles. We consider two types of such interactions: lubrication and contact.

Lubrication is there to compensate for the finite resolution of the flow simulation. When the surfaces of two particles get within a distance $\approx \Delta$, the grid cannot resolve the flow and the associated forces between the two particles anymore. This is compensated for by applying a radial (i.e. normal to the particle surfaces), equal but opposing force on each of the two particles. Given that the overwhelming majority of the contacts between spherical rings are between spherically shaped surfaces, we use analytical expressions for the strength of such lubrication forces [Kim and Karrila, 1991]: $F_{lub} = \frac{3}{8}\pi\rho\nu d^2\, \mathbf{n} \cdot \mathbf{\Delta u}_m / s$ with $\mathbf{n}$ the unit normal direction (defined in a more detailed way in [Derksen, 2019]), $\mathbf{\Delta u}_m$ the relative velocity of the two marker points, and s their spacing in normal direction. Based on analyses in [Kim and

Karrila, 1991], we do not consider the significantly weaker tangential lubrication forces. In the simulations, the expression above for the lubrication force is amended in two ways: (1) s^{-1} is replaced by $s^{-1}-\Delta_{lub}^{-1}$ with Δ_{lub} the threshold distance for lubrication so as to "switch on" lubrication smoothly [Nguyen and Ladd, 2002]; and (2) if $s \le s_{sat}$ the lubrication force saturates, so as to avoid high force levels and (numerical) instability. In the present study $\Delta_{lub}=\Delta$ and $s_{sat}=0.1\Delta$.

Contact forces are there to mimic "dry" contact between particles and thus to avoid their volumes to overlap. These are repulsive linear spring forces that depend on the normal distance (and – as opposed to lubrication forces – not on the relative velocity) between marker points of two different particles. When the normal distance between two marker points on two different particles falls below 0.075Δ the spring gets activated. Also here only normal forces are considered, i.e. the dry contact does not include friction, i.e. surfaces are smooth.

The dynamics of the (rigid) particles is governed by Newton's and Euler's equation for linear and rotational motion respectively. These equations are solved with the same time step Δt as the LB updates. To achieve stability of time stepping for the solids dynamics we use a split-derivative method [Shardt and Derksen, 2012] for discretizing the time derivatives in the equations of motion. Once linear velocities of particles have been updated their location is updated by an Euler-forward method; once angular velocities have been updated the evolution of the orientation of the particles is updated in terms of their quaternions [Kuipers, 1999].

The most relevant numerical settings are the lattice spacing Δ and the time step Δt. The lattice spacing is such that $d=16\Delta$; the time step is such that $\sqrt{\nu\Delta t}\big/d=8.84\cdot10^{-3}$. These resolutions produce reliable results based on grid-convergence tests we have carried out in the past for similar fluidized systems, mostly with solid spherical particles [Ten Cate et al.,2002; Derksen and Sundaresan, 2007]. The initial condition for each simulation is a domain containing a random (in terms of location and orientation) arrangement of non-overlapping particles at a certain packing fraction, and liquid, all at rest. Once gravity and the body force on the liquid are initialized, the systems evolve towards a steady state which – as we will see – takes of the order of $t\nu/d^2 \approx 3$ which translates in approximately $4\cdot10^4\Delta t$. Subsequently we run the system for another $4\cdot10^4\Delta t$ steps to collect data for statistical processing.

Figure 3 shows time series of average vertical velocities for one sample case. Steady velocities are reached very quickly after startup; later in this paper it is demonstrated that wave instabilities need much longer to develop. Particles on average move down, whereas interstitial liquid moves up. From a practical fluidization perspective the average mixture velocity $\overline{u}_{mz}$ relative to the average solids velocity $\overline{u}_{pz}$ is most relevant: $\overline{u}_{mz}-\overline{u}_{pz}=\left(1-\langle\phi\rangle\right)\left(\overline{u}_{\ell z}-\overline{u}_{pz}\right)$ (with $\overline{u}_{\ell z}$ the interstitial liquid velocity) as it is the vertical superficial velocity observed in a fluidization experiment with the particles on average not traveling vertically. The way the associated Reynolds number $\mathrm{Re}=\left(1-\langle\phi\rangle\right)\left(\overline{u}_{\ell z}-\overline{u}_{pz}\right)d/\nu$ depends on spherical ring type and packing fraction for $\mathrm{Ar}=5.64\cdot10^3$ and $\mathrm{Ar}=1.13\cdot10^4$ is shown in Figure 4 where it should be noted that the net weight of particles having the same Archimedes number is the same. The average superficial velocity decreases with increasing packing fraction and slightly increases with increasing bore diameter. For reference, the figure also shows results for solid spheres (i.e. results with $d_i=0$) for the two Archimedes numbers.

4. RESULTS

4.1 Waves, wave speed & wave form

As alluded to already, the fluidized systems develop wave instabilities under the given range of conditions. Previously – for solid spheres – these wave characteristics were used for validation and verification of the simulation method; by mimicking an experimental case due to Duru et al [Duru et al., 2002] (their case “Combination 7”) we were able to reproduce the correct wave speed (within 10%) and waveform [Derksen and Sundaresan, 2007; Derksen, 2023]. The simulated dimensionless wave speed (c) for solid spheres at a solids volume fraction of $\langle\phi\rangle=0.50$ and at $\mathrm{Ar}=5.63\cdot10^3$ was $cd/\nu=33.3$. We use this as a reference value to compare with the wave speeds obtained with spherical rings at similar Archimedes numbers and packing fractions.

Figure 5 shows an example of how the flow is being analyzed in terms of its wave behavior. The instantaneous realizations show a side view and a cross section through the simulation. From the cross section (Figure 5b) it becomes clear that the solids volume fraction has a large-scale variation with *z*; a less dense region is visible at around two-thirds of the height in that panel. This voidage region travels in the positive *z*-direction as shown in the space-time plot of the solids volume fraction (Figure 5c). The wave needs some time to develop; it reaches a steady state at about $t\nu/d^2 \approx 3$ after startup from zero velocities. From Figure 5c we can derive a wave speed s. By shifting the solids volume fraction profiles $\phi(z,t)$ to $\phi(z-st,t)$ (and applying periodicity in the *z*-direction) – as we do in Figure 5d – the waveform becomes apparent (Figure 5e). The wave speed s is in a fixed reference frame that sees a net motion of solids in the negative *z*-direction (see Figure 3). To compare with an experiment (that usually has no net vertical solids motion), the wave speed c one would measure needs to be compared to our simulated wave speed relative to the particle motion; $c = s - \overline{u}_{pz}$ with $\overline{u}_{pz}$ the (negative) average particle velocity. The amplitude of the wave depends strongly on the overall solids volume fraction as is shown in Figure 6. With less space for liquid-rich voids to develop, the higher packing fractions have smaller amplitude waves.

4.2 Flow through bores

To achieve solid-liquid mass transfer inside the bores of the spherical rings one needs flow through the cylindrical bores. Given the driving forces (gravity down and body force / pressure gradient up) it is expected that the orientation of the bores has relevance; vertical bores will have more opportunity for through-flow than horizontal ones. For this reason we study the orientation distributions of the spherical rings in Figure 7, where we compare the three bore diameters mentioned above. It shows probability density functions (pdf's) of the angle ψ between the bore centerline and the vertical direction collected from 500 instantaneous particle realizations over a time period of $3.91\nu/d^2$. An isotropic random distribution has a pdf equal to $\sin\psi$; many possibilities for horizontal oriented bores ($\psi \approx \pi/2$), less so for vertical ones ($\psi \approx 0$). Figure 7 shows that the spherical rings with the widest bores closely follow the $\sin\psi$ distribution. For the narrower bores, however, ψ's near $\pi/2$ are over-represented, and near 0 under-represented which means they tend more towards horizontal orientation. It is not directly clear what causes this distinction between the different bore diameters. As a reference we conducted tests of settling one spherical ring particle. This consistently led to it evolving to $\psi = \pi/2$ for all three d_i/d ratios investigated in this paper and thus was not very informative for explaining the trends in Figure 7. Clearly, strong direct and hydrodynamic interactions between particles lead to a spectrum of orientations with the single-particle settling simulations at best explaining some preference for $\psi = \pi/2$.

The impact of the Archimedes number on the orientation distribution is given in Figure 8 (top row of panels). The trend is a stronger departure from random isotropy for higher Archimedes numbers, i.e. for more vigorous fluidization. In addition, Figure 8 (bottom row) shows the strength of flow through the bores. Here, the velocity $\langle u_1 \rangle$ is the average flow in the x_1-direction (which is the bore centerline direction) relative to the particle velocity in that direction. The results show that the through-flow is highly correlated with the particle orientation; vertically oriented bores having stronger flow, which was anticipated. In addition, the strength of the through-flow closely follows a linear relationship with the Archimedes number.

The flow through the bores also correlates with the voidage waves. Figure 9 shows that the through-flow is stronger in the trough of the wave and weaker in its denser part. The cases in Figure 9 are those for which wave form and amplitude were presented in Figure 6 and show that higher amplitude waves overall lead to more flow through the bores.

Previously [Derksen, 2023] we have argued that the flow through bores (then in cylinders rather than in spheres) resembles Poiseuille flow. In instantaneous realizations of the flow system, the volume-averaged velocity $\langle u_1 \rangle$ in each particle is compared to the average velocity $\langle u_{p1} \rangle$ that would follow from the driving force at that same moment for flow through the bore based on the Poiseuille flow expression.

The force driving the flow through a bore has two contributions: the pressure gradient that we take as the pressure difference between the two ends (a and b with $z_a \le z_b$) of the bore divided by h, $\Gamma_1 = \frac{p_a - p_b}{h}$; and the component along the x_1-direction of the upward body force $\mathbf{f}$ acting on the fluid, $|\mathbf{f}|\cos\psi$. Then (assuming Poiseuille flow) $\langle u_{p1}\rangle = \frac{\left(|\mathbf{f}|\cos\psi + \Gamma_1\right) d_i^2}{32\rho\nu}$. Figure 10 gives evidence that $\langle u_1\rangle$ and $\langle u_{p1}\rangle$ on many occasions closely relate and it is concluded that for the purpose of estimating mass transfer at the bore surfaces it is fair to hypothesize Poiseuille flow there.

4.3 Consequences for mass transfer at bore surfaces

The mass transfer analysis will be based on Fick diffusion in the liquid phase along with Poiseuille flow in the cylindrical bore with diameter d_i and length h. The diffusivity κ is taken such that the Schmidt number $\mathrm{Sc} = \nu/\kappa = 1\cdot 10^3$. If the residence time of the liquid in the bore is sufficiently small, the mass penetration depth is very much smaller than d_i and analytical solutions to the mass concentration profiles can be applied to estimate mass transfer rates [Deen, 1998]. In the cases considered here, short residence time implies $\frac{\kappa h}{|\langle u_1\rangle| d_i^2} < 0.05$. If this condition is met and in the presence of Poiseuille flow $\mathrm{Sh} = 1.62\left(\frac{|\langle u_1\rangle| d_i^2}{\kappa h}\right)^{1/3}$ with Sh the Sherwood number defined as $\mathrm{Sh} = k d_i/\kappa$ with k the mass transfer coefficient. This goes by the name of Graetz solution or Graetz correlation [Deen, 1998]. Averaging this over all particles in a simulation and over many instantaneous realizations leads to average Sherwood numbers and average mass transfer coefficients $\langle \mathrm{Sh}\rangle = \langle k\rangle d_i/\kappa$. While averaging we discarded the instances (less than 1%) for which the short-time criterion was not met.

Average Sherwood number data is presented in Figure 11, where we have tried to visualize three overall dependencies. The first is an – obvious – increase of $\langle \mathrm{Sh}\rangle$ with the Archimedes number which means that if fluidization is more vigorous, mass transfer in the bores increases. The second is an increase of $\langle \mathrm{Sh} \rangle$ with increasing bore diameter relative to spherical ring diameter d_i/d. This is the result of a stronger flow through the bores but also of the definition of the Sherwood number which is directly proportional to d_i. The third – less straightforward – trend is an increase of $\langle \mathrm{Sh} \rangle$ with decreasing packing fraction $\langle \phi_{pck} \rangle$. For the widest bore this trend is clear, for the less wide ones it is less clear or even absent. The trend is likely related to the stronger wave amplitudes observed for the lower packing fractions, instigating more vigorous motion in the voids.

A perhaps more meaningful way of comparing mass transfer performance between the configurations we investigated is in terms of mass transfer rate per unit volume, i.e. consider the product of mass transfer coefficient and available mass transfer surface area per unit volume. In textbooks [Bird et al., 2015] this usually goes by $k_L a$.

The average Sherwood number is defined as $\langle \mathrm{Sh} \rangle = \langle k \rangle d_i/\kappa$ so that the average mass transfer coefficient is $\langle k \rangle = \kappa \langle \mathrm{Sh} \rangle / d_i$. Given that mass transfer is limited to the surface of the bores, transfer area per unit volume is $a = \frac{n\pi h d_i}{nx \cdot ny \cdot nz}$ so that $\langle k \rangle a = \frac{n\kappa \langle \mathrm{Sh} \rangle \pi h}{nx \cdot ny \cdot nz}$. If we scale $\langle k \rangle a$ with the viscous time-scale d^2/ν we get the dimensionless expression $\langle k \rangle a\, d^2/\nu = 6\langle \phi \rangle \frac{\langle \mathrm{Sh} \rangle}{\mathrm{Sc}} \frac{d^2}{d^2 - d_i^2}$. This is because $h^2 = d^2 - d_i^2$ and $V_p = \frac{\pi}{6} h^3$. This dimensionless quantity we use – as an alternative to the average Sherwood number – to compare mass transfer performance of our different configurations in Figure 12. The trends of this quantity give a slightly different picture as compared to the trends for $\langle \mathrm{Sh} \rangle$; $\langle k \rangle a\, d^2/\nu$ (still) increases with increasing Ar. The differences between the packing fractions are less than for $\langle \mathrm{Sh} \rangle$. Most noteworthy are perhaps the trends with d_i/d. Where for $\langle \phi_{pck} \rangle$=0.494 mass transfer increases with increasing d_i, for $\langle \phi_{pck} \rangle$=0.583 the widest bores (d_i/d=0.608) are overtaken by d_i/d=0.487 in terms of mass transfer performance. The reason for this is geometrical; the interfacial area per unit volume is larger for the narrower bores. This can be appreciated through the expression $\langle k\rangle a\, d^2/\nu = 6\langle\phi\rangle \frac{\langle \mathrm{Sh}\rangle}{\mathrm{Sc}} \frac{d^2}{d^2-d_i^2}$. Geometrically the bores d_i/d =0.608 and 0.487 differ through $\langle\phi\rangle \frac{d^2}{d^2-d_i^2} \propto \sqrt{d^2-d_i^2}$. The latter factor is about 10% larger for the narrower bore which then more than compensates for its lower $\langle \mathrm{Sh}\rangle$.

5. CONCLUSIONS

In this paper we assessed the mass transfer performance of dense systems of liquid-fluidized spherical ring particles by means of detailed numerical simulations. Mass transfer was supposed to be restricted to the surface of the cylindrical borehole in the sphere. The simulations resolved the flow around individual particles with the particle motion governed by hydrodynamic forces, including short-range lubrication forces, collisions between particles, gravity (down) and a body force (up) on the fluid representing a pressure gradient. The conditions, mainly defined through an Archimedes number and packing fraction, were such that wave type instabilities develop. It was shown that the wave amplitude strongly depends on the packing fraction. It was also shown that the waves in spherical rings fluidization have speeds comparable to fluidized solid spheres at comparable Archimedes numbers.

Dependent on the aspect ratio of the spherical rings – d_i/d with d the sphere diameter and d_i the bore diameter – the rings orient slightly differently with respect to the direction of gravity. The relevance of this is that orientation was shown to closely correlate with the strength of the flow through the bores which – in turn – is the motor for mass transfer; vertical orientation of the bore has much stronger though-flow than horizontal orientation. The waves also correlate with mass transfer. In the void parts of the waves, particle motion is more vigorous which results in stronger flow though the bores.

The mass transfer performance of the fluidized systems was quantified by an overall average Sherwood number $\langle \mathrm{Sh}\rangle = \langle k\rangle d_i/\kappa$ and by a volumetric $k_L a$-type coefficient. The latter was scaled to the dimensionless quantity $\langle k\rangle a\, d^2/\nu$. For $\langle \mathrm{Sh}\rangle$ the following trends were observed: it increases with increasing Archimedes number, with increasing bore diameter relative to sphere diameter and with decreasing packing fraction. For $\langle k \rangle a\, d^2 / \nu$ the trends were a little more subtle. There only was a weak dependency on the packing fraction while – under certain circumstances – narrower bores performed better than wider ones.

There is no doubt that experimentation will need to be performed in order to assess the quality of the trends observed through the simulations presented here. Although the simulations likely capture a good deal of the flow physics, some of the modeling steps – most prominently the dealings with close-range particle-particle interactions – need guidance through experimental results.

Another avenue of future work is scalar transport simulation for estimating mass transfer rates. In the current paper, mass transfer is calculated based on a (to a good level justified) Poiseuille flow assumption for the bore flow. That assumption could be further assessed by solving a passive scalar equation coupled with the liquid flow (as in e.g. [Derksen, 2014]). A major challenge – and reason why it has not been done in this paper – for this would be dealing with the high demand for spatial resolution of the scalar transport solver at the high Schmidt numbers ($\mathrm{Sc} \approx 10^3$) in liquids resulting in very thin concentration boundary layers at the bore surface.

References

Adelusi, I., Chiemela Victor, A., Andrieux, F., Dawson, R., 2020, Practical development of a ZnBr2 flow battery with a fluidized bed anode Zinc-electrode. J. Electrochemical Soc. 167, 050504, https://doi.org/10.1149/2.0112005JES.

Bartholomew, C., 2001, Mechanisms of catalyst deactivation. Applied Catalysis A: General 212, 17–60.

Bird, R.B., Stewart, W.E., Lightfoot, E.N., Klingenberg, D.J., 2015, Introductory transport phenomena. Wiley, Hoboken.

Clift, R., Grace, J.R., Weber, M.E., 1978, Bubbles, drops and particles. Academic Press, New York.

Deen, W.M., 1998, Analysis of transport phenomena. Oxford University Press, New York.

Derksen, J., Van den Akker, H.E.A., 1999, Large eddy simulations on the flow driven by a Rushton turbine. AIChE J. 45, 209–221.

Derksen, J.J., Sundaresan, S., 2007, Direct numerical simulations of dense suspensions: wave instabilities in liquid-fluidized beds. J Fluid Mech. 587, 303–336, https://doi.org/ 10.1017/S0022112007007094.

Derksen, J.J., 2014, Simulations of solid-liquid mass transfer in fixed and fluidized beds. Chem. Eng. J. 255, 233–244, http://dx.doi.org/10.1016/j.cej.2014.06.067.

Derksen, J.J., 2019, Liquid fluidization with cylindrical particles: Highly resolved simulations. AIChE J. 65, e16594, https://doi.org/10.1002/aic.16594.

Derksen, J.J., 2023, Liquid fluidization of short hollow cylinders. Ind. Eng. Chem. Res. 62, 19197−19204, https://doi.org/10.1021/acs.iecr.2c04464.

Duru, P, Nicolas, M., Hinch, J., Guazzelli, E., 2002, Constitutive laws in liquid-fluidized beds. J. Fluid Mech. 452, 371–404, https://doi.org/10.1017/S0022112001007017.

Eggels, J.G.M., Somers, J.A., 1995, Numerical simulation of free convective flow using the lattice-Boltzmann scheme. Int. J. Heat Fluid Flow. 16, 357–364.

Froment, G.F., Bischoff, K.B., De Wilde, J., 2011, Chemical reactor analysis and design, 3rd edition. Wiley, Hoboken.

Kim, S., Karrila, S.J., 1991, Microhydrodynamics: Principles and selected applications. Butterworth–Heinemann, Boston.

Koerich, D.M., Machado da Rosa, L., 2021, Analysis of hydrodynamic effects on biofilm thickness in fluidized-bed tapered bioreactors. Particuology 58, 48–57, https://doi.org/10.1016/j.partic.2021.01.011.

Kuipers, J.B., 1999, Quaternions and Rotation Sequences. Princeton University Press, Princeton.

Kunii, D., Levenspiel, O., 1993, Fluidization Engineering, 2nd edition. Butterworth-Heinemann, Boston.

Nguyen, N-Q., Ladd, A.J.C., 2002, Lubrication corrections for lattice-Boltzmann simulations of particle suspensions. Phys. Rev. E. 66, 046708, https://doi.org/10.1103/PhysRevE.66.046708.

Pronk, P., Infante Ferreira, C.A., Witkamp, G.J., 2006, Influence of solute type and concentration on ice scaling in fluidized bed ice crystallizers. Chem. Eng. Sc. 61, 4354 – 4362, https://doi.org/10.1016/j.ces.2006.02.019.

Rubinstein, G.J., Derksen, J.J., Sundaresan, S., Lattice Boltzmann simulations of low-Reynolds-number flow past fluidized spheres: effect of Stokes number on drag force. J. Fluid Mech. 788, 576–601, https://doi.org/10.1017/jfm.2015.679.

Seepma, S.Y.M.H., Koskamp, J.A., Colin, M.G., Chiou, E., Sobhan, R., Bogels, T.F.J., Bastiaan, T., Zamanian, H., Baars, E.T., de Moel, P.J., Wolthers, M., Kramer, J.I., 2025, Mechanistic model advancements for optimal calcium removal in water treatment: Integral operation improvements and reactor design strategies. Water Research 268, 122781–1–12, https://doi.org/10.1016/j.watres.2024.122781.

Shardt, O., Derksen, J.J., 2013, Direct simulations of dense suspensions of non-spherical particles. Int J Multiphase Flow. 47, 25–36, http://dx.doi.org/10.1016/j.ijmultiphaseflow.2012.06.007.

Somers, J.A., 1993, Direct simulation of fluid flow with cellular automata and the lattice-Boltzmann equation. Appl. Sc. Res. 51, 127–133.

Succi, S., 2001, The lattice Boltzmann equation for fluid dynamics and beyond. Clarendon Press, Oxford, Sundaresan, S., 2003, Instabilities in fluidized beds. Annu. Rev. Fluid Mech. 35, 63–88, https://doi.org/10.1146/annurev.fluid.35.101101.161151.

Syed, N.H., Dickinson, J.E., Galvin, K.P., Moreno-Atanasio, R., 2018, Continuous, dynamic and steady state simulation of the reflux classifier using a segregation-dispersion model. Minerals Engineering 115, 53–67, https://dx.doi.org/10.1016/j.mineng.2017.10.010.

Ten Cate, A., Nieuwstad, C.H., Derksen, J.J., Van den Akker, H.E.A., 2002, PIV experiments and lattice-Boltzmann simulations on a single sphere settling under gravity. Phys Fluids. 14, 4012–4025, https://doi.org/ 10.1063/1.1512918.

Van der Hoef, M.A., Beetstra, R.,Kuipers, J.A.M., 2005, Lattice-Boltzmann simulations of low-Reynolds-number flow past mono- and bidisperse arrays of spheres: results for the permeability and drag force. J. Fluid Mech. 528, 233–254, https://doi.org/10.1017/S0022112004003295.

Van der Hoef, M.A., Ye, M., Van Sint Annaland, M., Andrews, A.T., Sundaresan, S., Kuipers, J.A.M., 2006, Multi-scale modeling of gas-fluidized beds. Adv. Chem. Eng. 31, 65-149, https://doi.org/10.1016/S0065-2377(06)31002-2.

Wen, C.Y., Yu, Y.H., 1966, Mechanics of fluidization. Chem. Eng. Prog. 62, 100–111.

Figures

Figure 1. Rendering of a spherical ring particle.

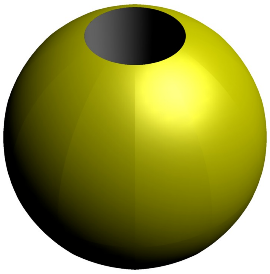

Figure 2. Spherical ring geometry and nomenclature of its main dimensions.

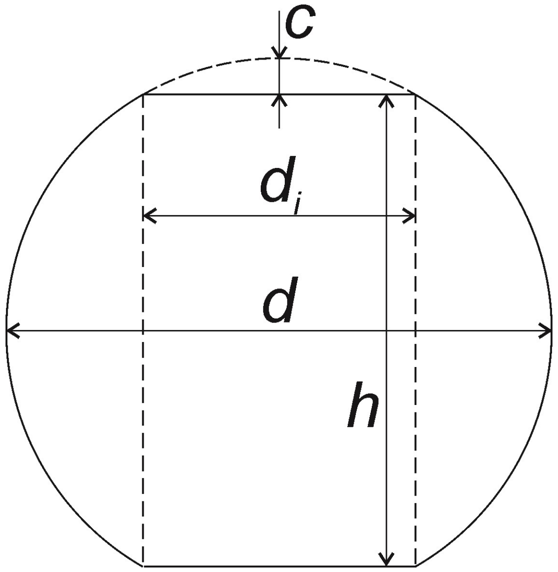

Figure 3. Sample time series of space-average vertical velocities ($\overline{u}_{\ell z}$ interstitial liquid velocity, $\overline{u}_{mz}$ mixture velocity, $\overline{u}_{pz}$ particle velocity) for $\langle \phi_{pck} \rangle = 0.537$, $d_i/d = 0.487$, Ar $=5.64 \cdot 10^3$. At $t=0$ particles and liquid have zero velocity.

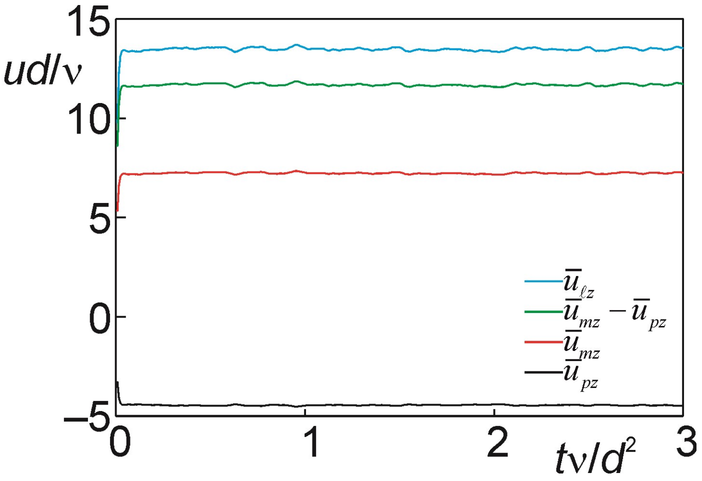

Figure 4. Reynolds number based on superficial fluidization velocity ($\mathrm{Re} = \left(1-\langle\phi\rangle\right)\left(\overline{u}_{\ell z}-\overline{u}_{pz}\right)d/\nu$) as a function of cylindrical bore diameter for various packing fractions as indicated at $\mathrm{Ar} = 5.64\cdot 10^3$ (filled symbols) and $\mathrm{Ar} = 1.13\cdot 10^4$ (open symbols). For reference date for solid spheres ($d_i = 0$) have been included.

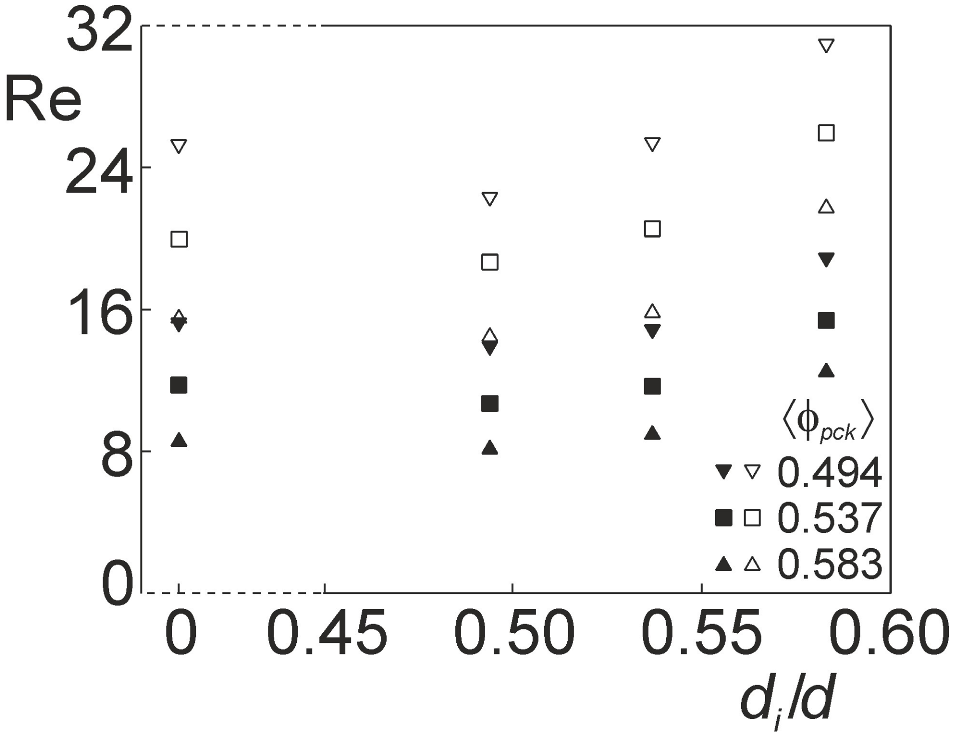

Figure 5. Results of a simulation with $\langle \phi_{pck} \rangle = 0.537$, $d_i/d = 0.608$, Ar $= 5.64 \cdot 10^3$. (a) Sideview snapshot at $t\nu/d^2 = 5.14$; (b) cross section snapshot at the same moment showing liquid velocity contours and particles with their center within distance d of the mid-plane; (c) space-time (z-t) plot of the solids volume fraction; (d) part of the z-t plot shifted by speed $s = 35.2\nu/d$, wave speed $c = s - \bar{u}_{pz} \approx 37.4\nu/d$; (e) time-averaged solids volume fraction wave profile.

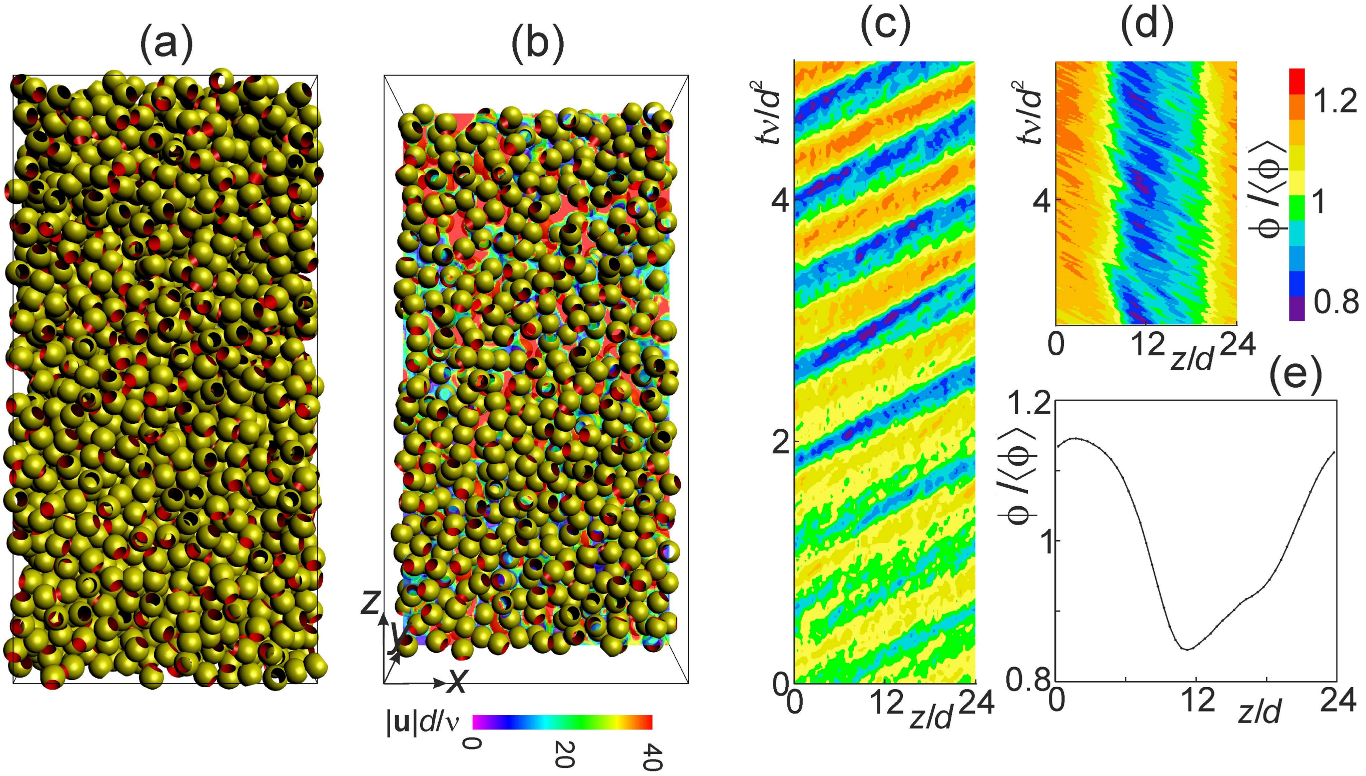

Figure 6. (a) Space-time (*z*-*t*) plot of solids volume fraction for $\langle \phi_{pck} \rangle = 0.494$, $d_i/d = 0.608$, $\mathrm{Ar} = 5.64 \cdot 10^3$; (b) idem for $\langle \phi_{pck} \rangle = 0.583$; (c) resulting time-averaged waveforms for the packing fractions as indicated.

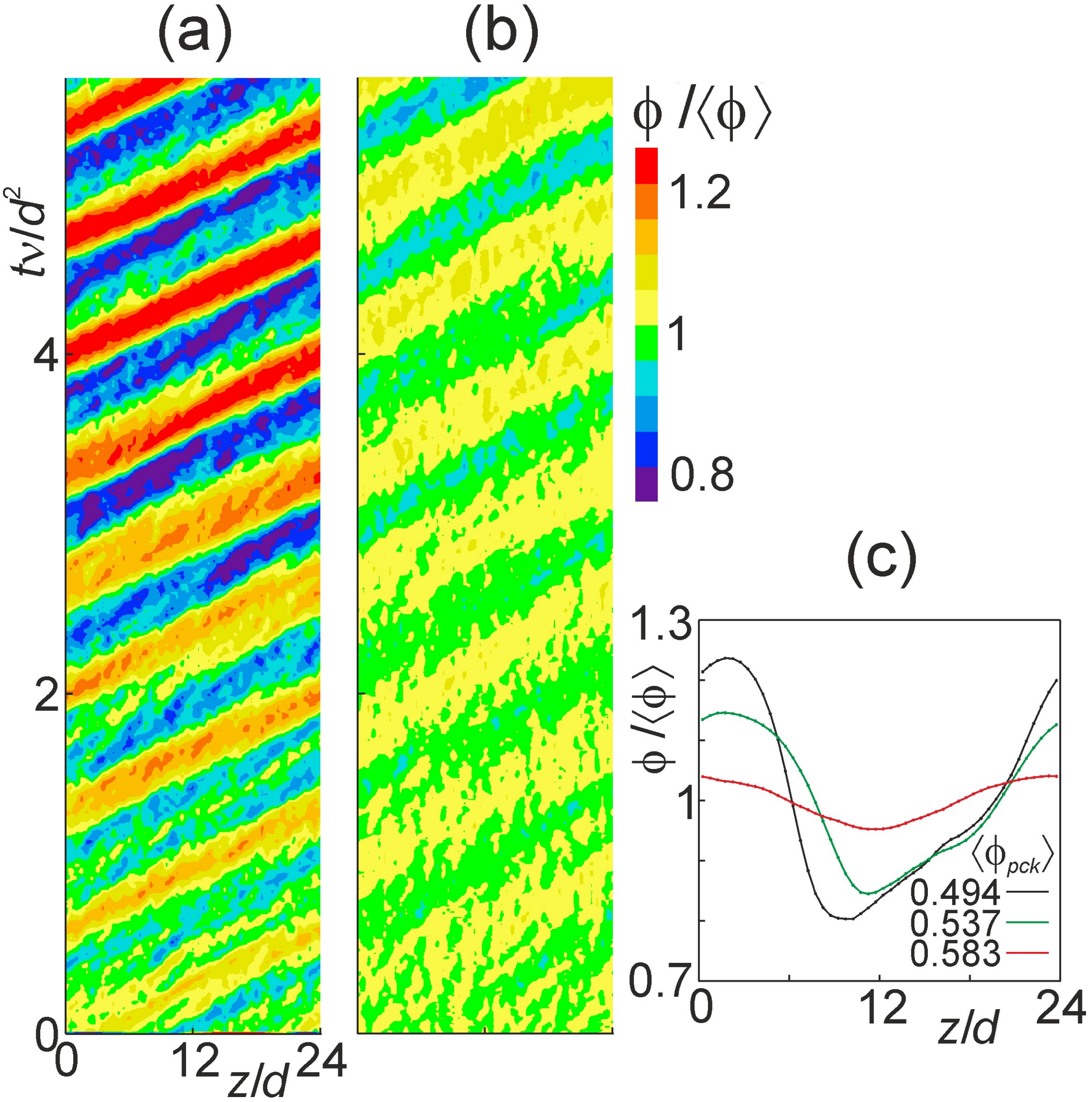

Figure 7. Distributions of the angle ψ of the bore centerline with the vertical at $\mathrm{Ar} = 5.64 \cdot 10^3$. Panels left to right: $d_i/d = 0.418$, 0.487 and 0.608 respectively; panels bottom to top $\langle \phi_{pck} \rangle = 0.494$, 0.537 and 0.583 respectively. Drawn curves are $\sin\psi$.

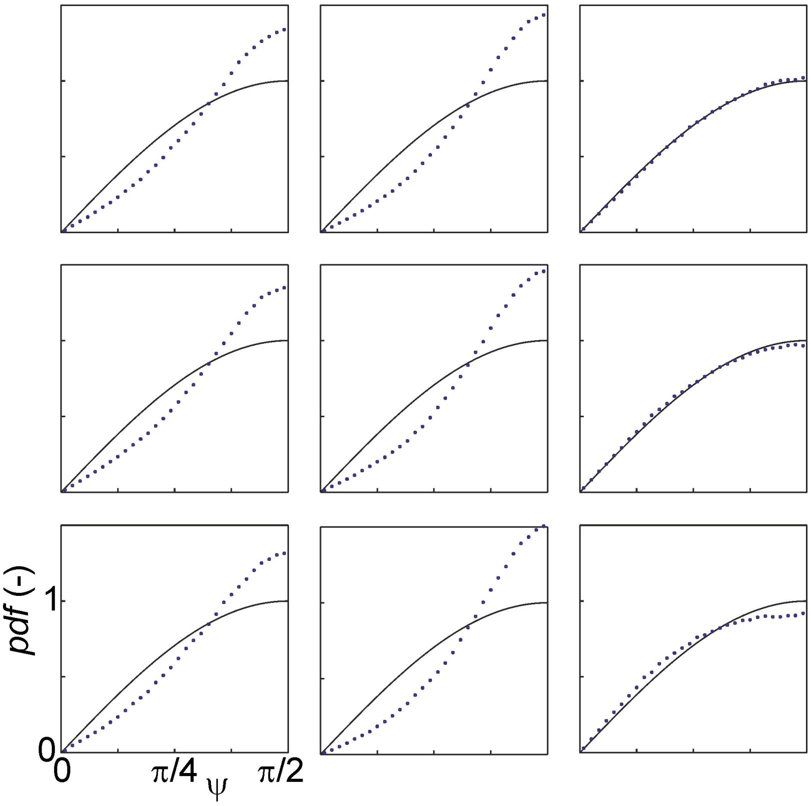

Figure 8. Top row: distributions of the angle ψ of the bore centerline with the vertical at – from left to right – Ar =2.82·10^3, 5.64·10^3 and 8.46·10^3 respectively; $d_i/d = 0.418$, $\langle \phi_{pck} \rangle = 0.537$. Drawn curves are $\sin\psi$. Bottom row: average Reynolds number of the flow through the bore conditional upon the angle ψ .

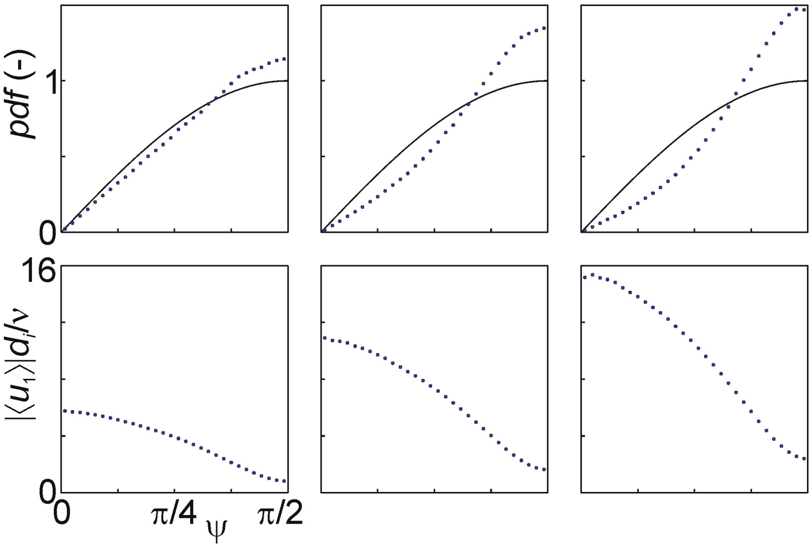

Figure 9. Space-time (*z*-*t*) plots of average Reynolds numbers $\left|\langle u_1\rangle\right| d/\nu$ in cylindrical bores for (a) $\langle\phi_{pck}\rangle = 0.494$, (b) $\langle\phi_{pck}\rangle = 0.537$,and (c) $\langle\phi_{pck}\rangle = 0.583$. $d_i/d = 0.608$ and Ar $=5.64\cdot10^3$.

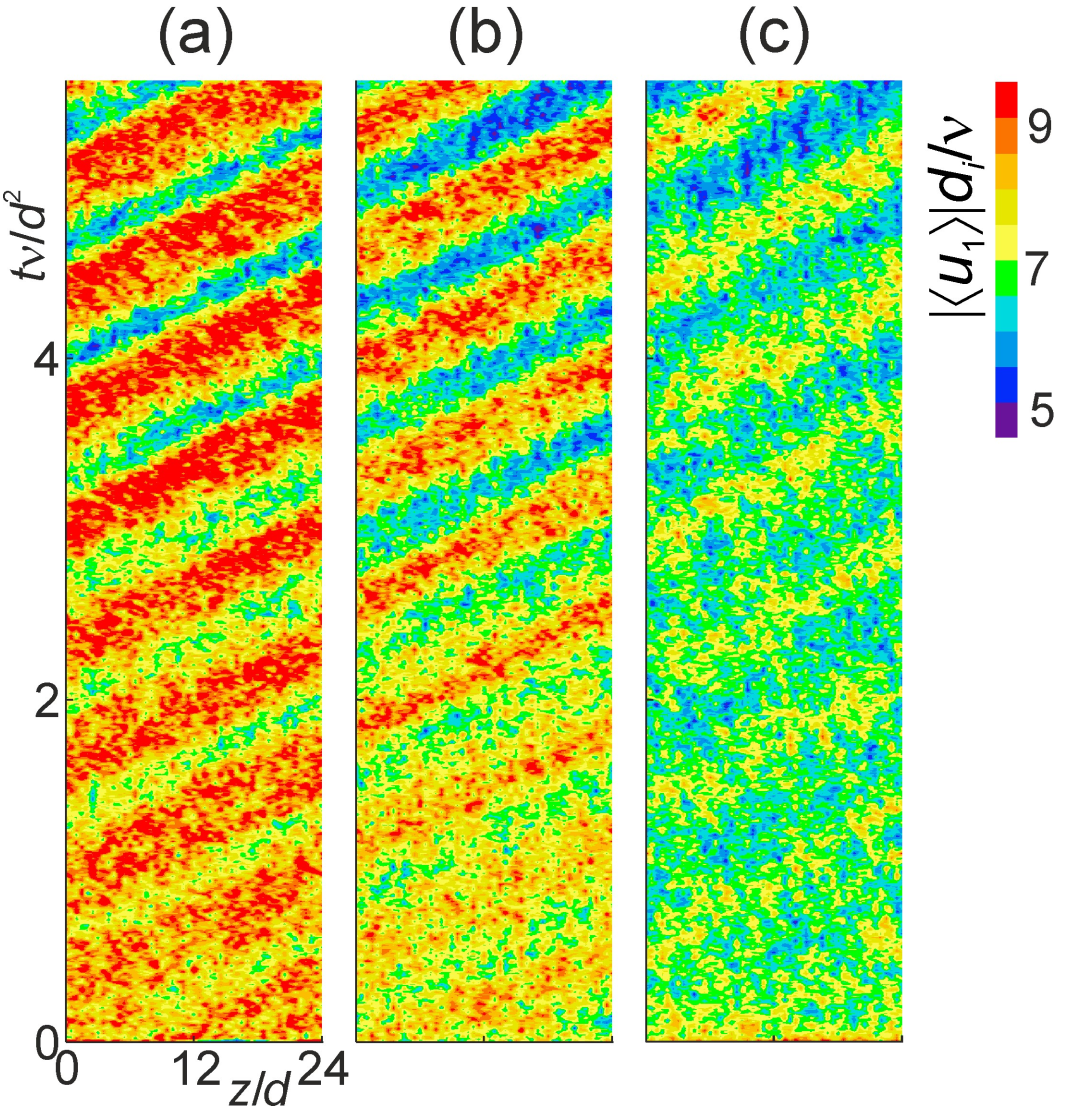

Figure 10. Average axial velocity $\langle u_1 \rangle$ in a cylindrical bore versus $\langle u_{p1} \rangle$ which is the average velocity calculated for Poiseuille flow from the driving force of flow in the bore. Each dot in each graph represents one spherical ring at a single moment in time. From left to right: $\mathrm{Ar} = 2.82 \cdot 10^3$, $5.64 \cdot 10^3$ and $8.46 \cdot 10^3$ respectively. Particles have $d_i / d = 0.487$, packing $\langle \phi_{pck} \rangle = 0.537$.

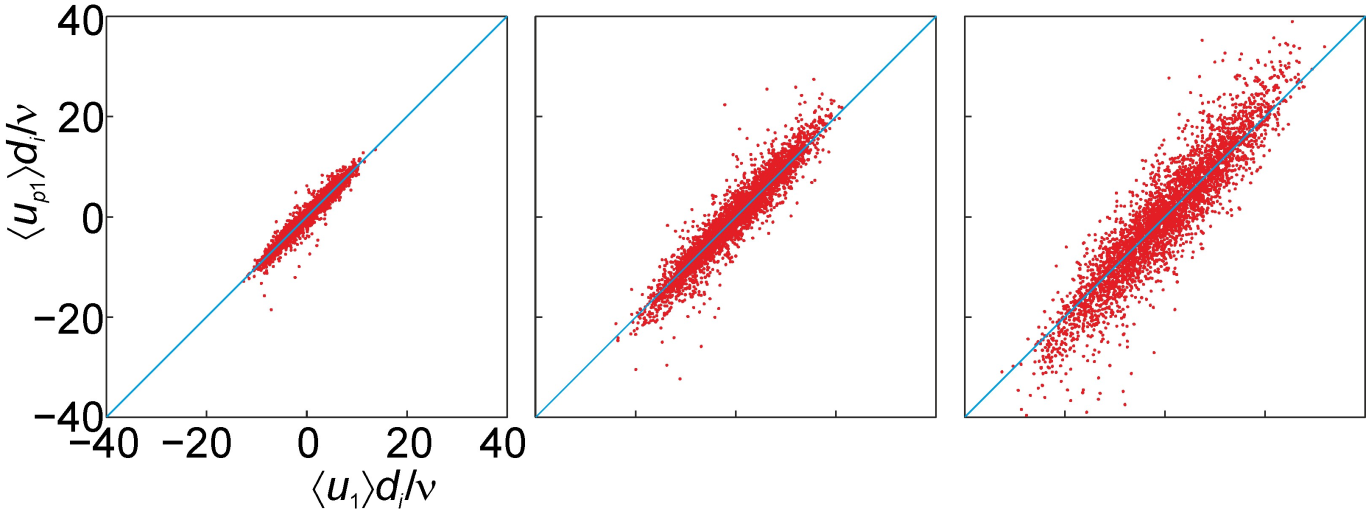

Figure 11. Average Sherwood number $\langle \mathrm{Sh} \rangle$ as a function of the Archimedes number Ar for the various values of $\langle \phi_{pck} \rangle$ and d_i/d as indicated.

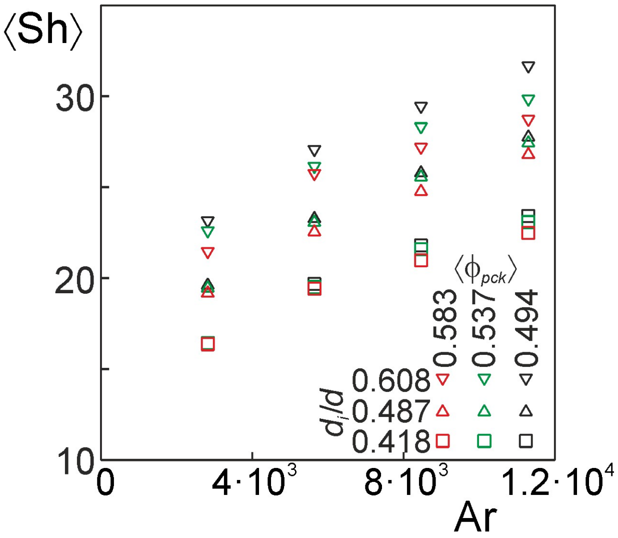

Figure 12. The volumetric mass transfer rate made dimensionless with viscous time $\langle k\rangle a\,d^2/\nu$ as a function of the Archimedes number for various spherical ring aspect ratios d_i/d and (from left to right) increasing packing fraction $\langle\phi_{pck}\rangle$.